

Article

Fabrication of Ni–MOF–74@PA–PEI for Radon Removal under Ambient Conditions

Xi Liu ^{1,2}, Yuan Sun ², Chunlai Wang ², Li Lv ^{2,*} and Yun Liang ^{1,*}¹ School of Light Industry and Engineering, South China University of Technology, Guangzhou 510640, China² State Key Laboratory of NBC Protection for Civilian, Beijing 102205, China

* Correspondence: shxllv@163.com (L.L.); liangyun@scut.edu.cn (Y.L.)

Abstract: Radon is one of the 19 carcinogenic substances identified by the World Health Organization, posing a significant threat to human health and the environment. Properly removing radon under ambient conditions remains challenging. Compared with traditional radon-adsorbent materials such as activated carbon and zeolite, metal-organic framework (MOF) materials provide a high specific surface area, rich structure, and designability. However, MOF material powders demonstrate complications regarding practical use, such as easy accumulation, deactivation, and difficult recovery. Ni–MOF–74 was in situ grown on a porous polyacrylic acid (PA) spherical substrate via stepwise negative pressure impregnation. Ni–MOF–74 was structured as one-dimensional rod-shaped crystals (200–300 nm) in large-pore PA microspheres, whose porous structure increased the diffusion of radon gas. The radon adsorption coefficient of a Ni–MOF–74@PA–polyethyleneimine composite material was 0.49 L/g (293 K, relative humidity of 20%, air carrier). In comparison with pristine Ni–MOF–74 powder, our composite material exhibited enhanced adsorption and longer penetration time. The radon adsorption coefficient of the composite material was found to be from one to two orders of magnitude higher than that of zeolite and silica gel. The proposed material can be used for radon adsorption while overcoming the formation problem of MOF powders. Our preparation approach can provide a reference for the composite process of MOFs and polymers.

Keywords: radon; metal-organic framework; Ni–MOF–74; polyacrylate; composite material; adsorption coefficient

**Citation:** Liu, X.; Sun, Y.; Wang, C.;Lv, L.; Liang, Y. Fabrication of Ni–MOF–74@PA–PEI for Radon Removal under Ambient Conditions. *Processes* **2023**, *11*, 1069. <https://doi.org/10.3390/pr11041069>

Academic Editor: Ioannis Spanopoulos

Received: 12 March 2023

Revised: 26 March 2023

Accepted: 29 March 2023

Published: 2 April 2023



Copyright: © 2023 by the authors. Licensee MDPI, Basel, Switzerland. This article is an open access article distributed under the terms and conditions of the Creative Commons Attribution (CC BY) license (<https://creativecommons.org/licenses/by/4.0/>).

1. Introduction

Radon (Rn) is an odourless and colourless radioactive noble gas primarily derived from soil, building materials, coal mining, and the nuclear industry. It has become a significant pollutant in underground, indoor, and mining environments [1]. When radon and its decay products attach to aerosols, dust, and smoke particles, they can enter the bronchial and lung tissues when breathed by humans, and the radioactive rays produced by their decay can irradiate human cells and organs, substantially increasing the risk of lung cancer and blood diseases [2–4]. Additionally, radon radioactivity interferes with rare-event search experiments, such as those involving neutrinos and dark matter. Hence, it is crucial to strictly control the concentration levels of radon in the environment [5–7].

The current measures for preventing and reducing the presence of radon mainly include adsorption, ventilation, sealing, and the design and renovation of buildings [8]. Adsorption is the most widely used technology for radon removal, and radon adsorption materials are decisive for effective removal. Moreover, the performance of such materials plays a critical role in improving the treatment efficiency, economic benefits, equipment reliability, and reducing environmental pollution. The common materials for radon adsorption include silica gel, molecular sieves, activated carbon, and metal-organic framework (MOF) materials. Early studies have shown that silica gel has a low radon adsorption coefficient under different carrier gas conditions, ranging from 0.0216 L/g to 0.0393 L/g [9].

Bikit et al. [10] measured the adsorption coefficient of natural zeolite samples between 0.038 L/g and 0.11 L/g. However, owing to the irregular pore size distribution and composition of natural zeolites and the difficulty of modifying the pore structure of synthetic zeolites, their radon adsorption properties are weak. Activated carbon is an adsorption material that has been used for many years, as it is reliable for radon adsorption in residential and commercial settings. Under average temperature and pressure conditions and with air as the carrier gas, the radon adsorption coefficients of activated carbon and its modified materials are generally between 3 L/g and 6 L/g [11–13]. However, the specific surface area and micropore quantity of activated carbon are limited, hindering the design and chemical modification of its structure. The demand for radon removal in engineering applications requires using a large amount of activated carbon [14].

MOFs have a rich microporous structure and high designability, providing an ideal storage space for various gases [15]. Thus, they have been widely used for the adsorption and the separation of inert gases [16–18]. Most studies on radon have used grand canonical Monte Carlo simulations and included the screening of MOFs and their absorption and separation of radon in mixtures such as Rn/Xe [19,20], Rn/N₂ [16,21], and Rn/O₂ [21,22]. The research group of Wang at Soochow University [22,23] was the first to experimentally study the radon adsorption performance of MOFs. They used grand canonical Monte Carlo simulations to screen the zeolitic imidazolate framework (ZIF) series of MOFs and obtained ZIF-7. Based on thermodynamics–kinetics–balanced principles, they adjusted the structure of ZIF-7 by replacing benzimidazole with imidazole, resulting in the preparation of ZIF-7-lm. At 293 K and a relative humidity of 25%, they measured the radon adsorption coefficient of ZIF-7-lm, increasing from 0 L/g to 8.6 L/g, surpassing that of activated carbon and demonstrating the potential of MOFs for radon adsorption.

M₂(DOBDC), or MOF-74 or CPO-27, is a coordination compound formed by combining metal ions such as Ni²⁺, Co²⁺, and Mg²⁺ with 2,5-dihydroxybenzoic acid (H₂DOBDC). This material possesses high-density open metal sites and exhibits excellent stability. Therefore, it has been extensively studied for gas adsorption and separation [24–26]. Perry et al. [16] used grand canonical Monte Carlo simulations and found that Ni-MOF-74 exhibits good selectivity towards radon in Rn/N₂ gas mixtures. As the molecular diameters of Xe (4.1 Å) and Rn (4.17 Å) are similar and they share similar physicochemical properties, MOFs for Xe adsorption may be effective for Rn adsorption. Theoretical calculations and experimental studies have shown that Ni-MOF-74 exhibits a better adsorption and selectivity towards Xe than other competitive gases [27,28]. At 1 bar and 298 K, Ni-MOF-74 has a Xe saturation adsorption capacity of 3.83 mol/kg, which is higher than that of activated carbon and HKUST-1 [29]. Thus, Ni-MOF-74 is a promising MOF for treating radioactive gas streams.

As a new type of adsorbent material, MOFs have broad application prospects. However, using powdered materials leads to compaction and deactivation, hindering efficient recovery. Thus, addressing MOF moulding is crucial for industrial applications. The most promising strategy toward the applicability of MOFs is forming composite materials with a substrate. Currently, the morphology of MOF composite materials mainly includes particles, films, or fibres. In addition, the primary composite processes include physical mixing, deposition precipitation, and in-situ growth [29–31]. Typically, the substrate materials are selected for MOFs from polymers, carbon materials, and silica. Remarkably, polymers have a wide variety of monomers and are highly designable, easy to process, and can be readily hybridised with MOFs through modification. Porous polyesters exhibit excellent mechanical properties, large pore structures promoting diffusion and mass transfer, and a spherical appearance, conducive to filling and fixing beds. Thus, they have great potential for practical engineering applications [32–34]. Therefore, MOFs@porous polymer composite materials have recently become a research hotspot.

We synthesised a polyacrylate (PA) spherical matrix material with a multilevel pore structure via emulsion polymerisation and improved the compatibility between PA and a MOF through amine functionalisation. Ni-MOF-74 was grown in situ on the large pore

surface of the matrix material via a stepwise impregnation to prepare the mechanically stable Ni–MOF–74@PA–polyethyleneimine (PEI) composite material. The morphology and structure of the material were characterised and analysed. Furthermore, a self–built experimental device was used to test the radon adsorption coefficient of Ni–MOF–74 and Ni–MOF–74@PA–PEI to investigate the adsorption performance of MOF and the new material system for radon.

2. Experimental Details

2.1. Materials

Polyvinyl alcohol 1788 (an alcoholysis degree of 87–89% mol/mol), ammonium persulfate (99%), tert–butyl methacrylate (99%), glycidyl methacrylate (97%), trimethylolpropane triacrylate (95%), toluene (AR), benzoyl peroxide (99.0%), N, N–dimethylaniline (99.0%), N, N, N', N'–tetramethylethylenediamine (99%), PEI (M.W. 1800), H₂DOBDC (98%), tetrahydrofuran (99%), and ethanol were purchased from Shanghai Macklin Biochemical Co., Ltd., Shanghai, China. Polyethylene glycol–polypropylene glycol–polyethylene glycol (PEG–PPG–PEG, M.W. 5800) was purchased from Sigma Aldrich (Shanghai) Trading Co., Ltd., Shanghai, China. Nickel acetate tetrahydrate (Ni(CH₃COO)₂·4H₂O, 99%) was purchased from Tianjin Heowns Biochemical Technology Co., Ltd., Tianjin, China. N₂ (≥99.999%) was purchased from Beijing Haipu Gas Co., Ltd., Beijing, China. All the chemicals were used without further purification.

2.2. Synthesis Method

2.2.1. Synthesis of PA and PA–PEI

The preparation of PA and PA–PEI is illustrated in Figure 1. For PA, the preparation method reported in [7,8] was used with slight modifications. The monomers tert–butyl methacrylate (1.4 g) and glycidyl methacrylate (4.6 g) and crosslinker trimethylolpropane triacrylate (4 g) were bathed in toluene (7.8 g), and the oil–soluble emulsifier PEG–PPG–PEG (1.4 g) and oxidant benzoyl peroxide (0.2 g) were added. The mixture was sonicated for 15 min to achieve a homogeneous oil phase. Under high–speed stirring at 3000 rpm, 30 mL of water was added dropwise to the oil phase within 5 min to form an emulsion. Then, the speed was changed to 6000 rpm for 6 min, and reducing agent N, N–dimethylaniline (10 drops) was added in the last 1 min. At 343 K and under an N₂ atmosphere, the prepared emulsion was poured into water (300 mL) containing dispersant polyvinyl alcohol (2 g) and ammonium persulfate (0.48 g). Then, the reducing agent N, N, N', N'–tetramethylethylenediamine (20 drops) was added. Under interfacial tension, the emulsion formed spherical particles in the third phase. The small spheres of 0.6–0.85 mm were sieved, washed with water, and soaked in methanol to remove the residual emulsifier in the material pores. Finally, the material was dried at 343 K to obtain the spherical porous polyacrylic acid ester–based material, PA.

For PA–PEI, PA (1.5 g) was placed in a round–bottom flask (250 mL) and the flask was sealed with a double–holed stopcock pressure–equalising dropping funnel and adapter. Then, PEI (50 g) and methanol (10 g) were thoroughly mixed by ultrasonication, and the mixture was added to the flask under vacuum. The mixture was heated at 403 K for 2 h under an N₂ atmosphere, and the resulting material was washed with methanol until neutralisation. Finally, the modified substrate material was vacuum dried at 353 K to obtain the PA–PEI.

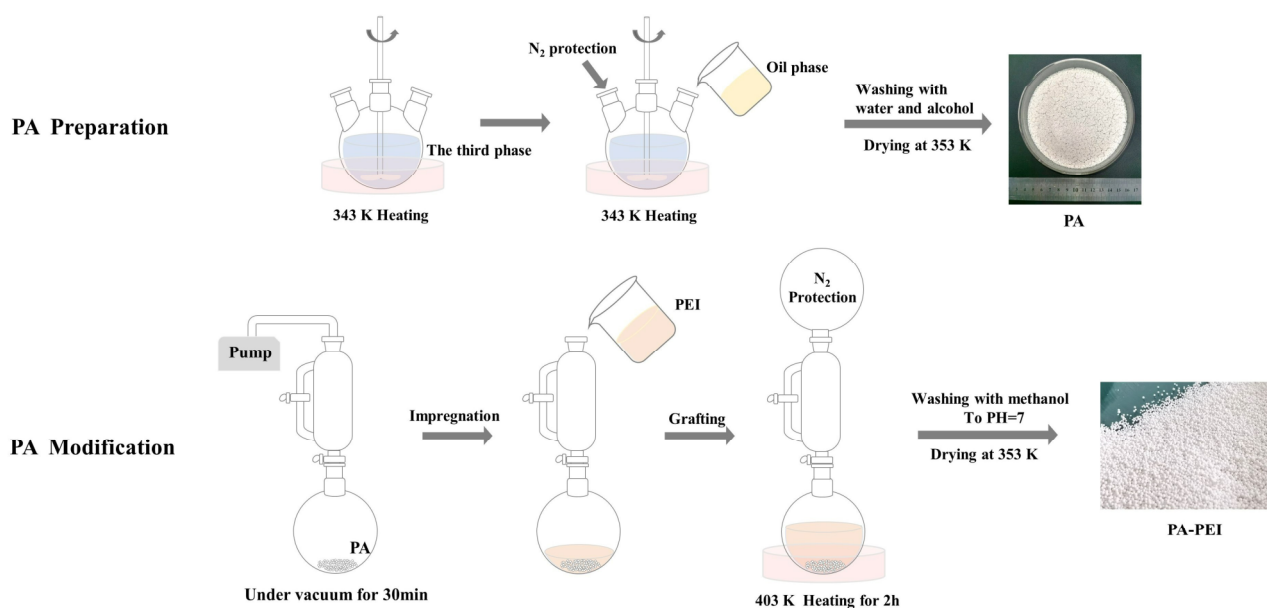


Figure 1. Schematic of the preparation of PA and PA–PEI.

2.2.2. Synthesis of Ni–MOF–74 and Ni–MOF–74@PA

The synthesis of Ni–MOF–74 was carried out using a hydrothermal method [25]. Nickel acetate tetrahydrate (3.73 g) was dissolved in ultrapure water (100 mL), and H₂DOBDC (1.49 g) was dissolved in tetrahydrofuran (100 mL). The two solutions were mixed and poured into a polytetrafluoroethylene–lined vessel, which was then sealed in a high–pressure reactor. After reacting in an oven at 383 K for 72 h, the upper liquid was removed. The product was washed several times with ethanol and deionised water. Finally, it was dried at 373 K in a vacuum oven for 12 h, resulting in a yellowish crystalline powder.

The preparation of Ni–MOF–74@PA–PEI is illustrated in Figure 2. PA–PEI (1.5 g) was placed in a 250 mL round–bottom flask, the flask was sealed with a double–jointed constant pressure dropping funnel and adapter, and vacuumed for 30 min. Then, Ni(CH₃COO)₂·4H₂O (7.46 g) was dissolved in ultrapure water (50 mL) as a precursor solution for negative pressure impregnation for 3 h. After the impregnation, the sample was dried in a vacuum–drying oven at 353 K. The PA–PEI–Ni²⁺ was vacuumed using the same method. The precursor solution was replaced with H₂DOBDC (1.98 g) dissolved in tetrahydrofuran (50 mL), and the mixture was transferred to a polytetrafluoroethylene–lined vessel sealed in a high–pressure reactor. After reacting at 383 K for 72 h in an oven, removed the liner, poured off the supernatant, repeatedly washed the product with water and ethanol, and then dried in a vacuum oven at 373 K for 12 h to obtain Ni–MOF–74@PA–PEI. The loading amount of Ni–MOF–74 in the composite material was 53.41 wt%. The calculation method is shown in the Supplementary Materials.

2.3. Characterisation

The crystal structure of the materials was characterised using an X–ray diffractometer (Ultima IV, Rigaku, Tokyo, Japan) with a Cu target and scanning range of 5–50° at a 2°/min. The functional groups of the material were characterised by measuring the absorbance within the range of 4000–400 cm^{−1} using a Fourier–transform infrared spectrometer (Nicolet iS20, Thermo Fisher Scientific, Waltham, MA, USA). The surface and cross–section of the materials were observed using a scanning electron microscopy (SEM) system (Gemini 300, ZEISS, Oberkochen, Germany). The valence states of the elements in the materials were measured using an X–ray photoelectron spectrometry (XPS) system (K–Alpha, Thermo Fisher Scientific, Waltham, MA, USA). The specific surface area, pore structure, and N₂ adsorption isotherms of the materials were analysed using an automated surface area and porosity analyser (Brunauer–Emmett–Teller—BET analysis, 3Flex, Micromeritics, Norcross,

GA, USA). The thermal stability of the materials was tested using a simultaneous thermal analyser (STA7300, Hitachi, Tokyo, Japan) under an N_2 atmosphere with a heating range of 303–1073 K at a rate of 5 K/min.

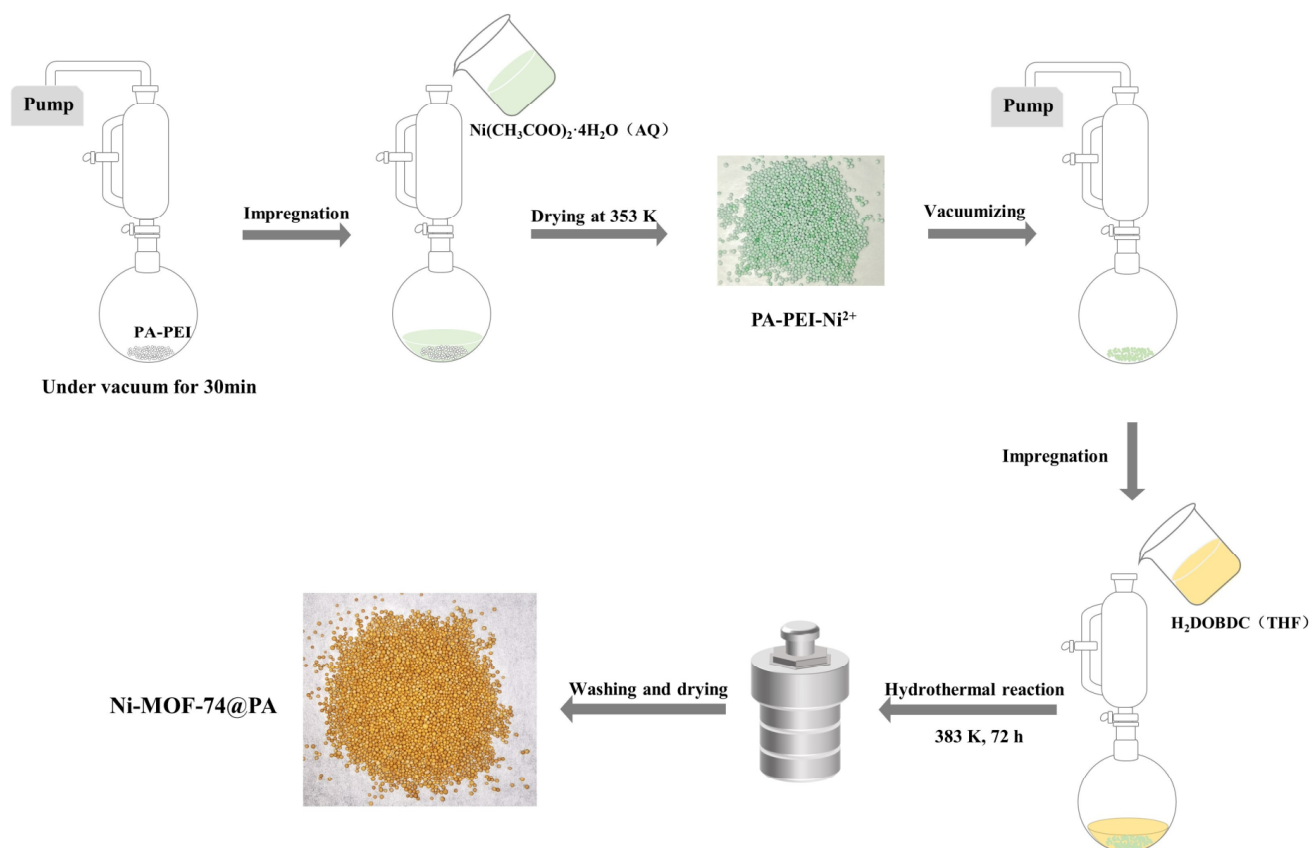


Figure 2. Schematic of the preparation of Ni–MOF–74@PA–PEI.

2.4. Radon Breakthrough Experiment

2.4.1. Experimental Setup

The laboratory measurement methods for the radon adsorption coefficient generally include three types: the static equilibrium method [13], the continuous air injection method [11,22], and the pulsed air injection method [35]. In this study, a radon gas penetration experimental apparatus was designed based on the principle of continuous air injection. The schematic of the apparatus is shown in Figure 3, where the black arrows indicate the direction of the gas flow. The radium ore from the State Key Laboratory of NBC Protection for Civilian was used as the radon source. A quartz tube with an inner diameter of 8 mm and length of 160 mm was used as the sample tube. The Rn concentration was detected using a portable radon detector (NRM–P01, Sairatec, Beijing, China), and the temperature and humidity during the experiment were recorded. The Rn concentration was measured and recorded every 5 min, and the instrument sensitivity was ≥ 0.8 cph/Bq/m³ with a detection limit of 2 Bq/m³. A polytetrafluoroethylene syringe filter was added to the instrument inlet to filter out the radon progeny, and a built-in pump of the radon detector promoted gas flow through the sample.

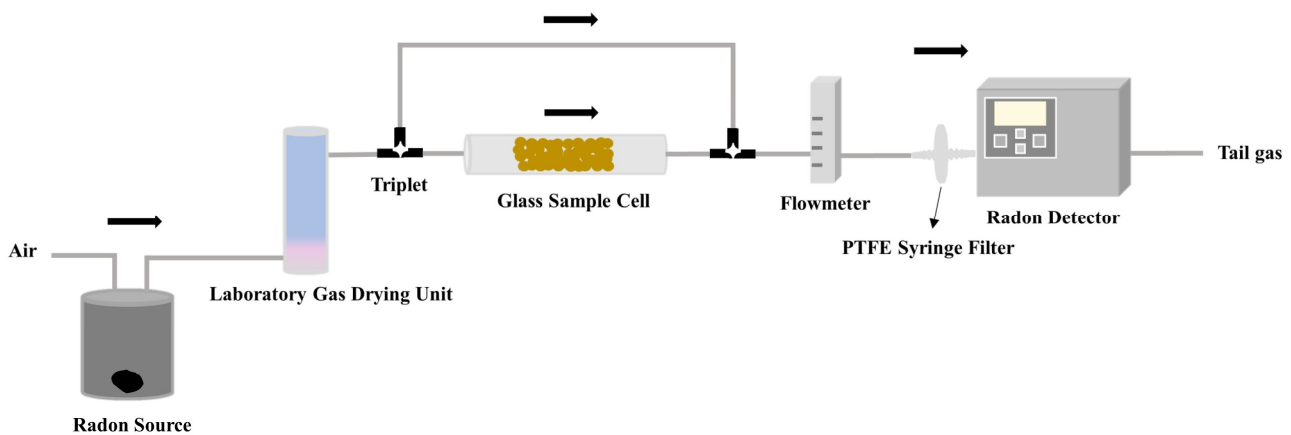


Figure 3. Schematic of the radon breakthrough experiment.

2.4.2. Test Preparation

Before testing the sample, the gas line was ventilated for 4–5 h to achieve an equilibrium of Rn concentration. The test result of Rn concentration over time without samples is shown in Figure 4, which indicates a relatively stable Rn concentration around 1920 Bq/m³. The gas concentration should be stable before testing the radon adsorption performance of the material. Then, the sample pipe containing the activated samples (in a vacuum oven at 423 K for 6 h) with quartz cotton on both ends was connected to the apparatus pipeline to begin adsorption. The dynamic adsorption experiment was completed when the Rn concentration returned to the initial concentration and remained at this level for at least 30 min.

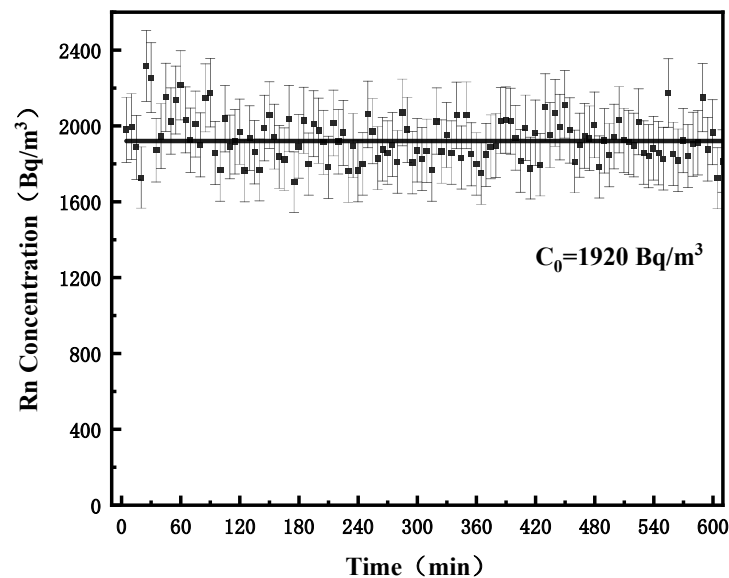


Figure 4. Rn concentration without samples over time.

2.4.3. Calculation of the Dynamic Adsorption Coefficients

The dynamic adsorption coefficient K_a (L/g) is commonly used to characterise the Rn capture capability of the adsorbents. The dynamic adsorption coefficient was calculated by the following equations [11,22]:

$$Q = \frac{1}{m} \int_0^t (C_0 - C_t) F dt \quad (1)$$

$$K_a = \frac{Q}{C_0} \quad (2)$$

where Q (Bq/g) is the radon activity adsorbed per unit mass of material, m (g) is the sample mass used in the penetration experiment, C_0 (Bq/m³) is the stable Rn concentration before testing the sample, C_t (Bq/m³) is the Rn concentration measured by a detector at time t , F (L/min) is the gas flow rate during the experiment, and t (min) denotes the experiment time.

3. Results and Discussion

3.1. Composition Analysis and Morphology Characterization

The X-ray diffraction patterns of the prepared materials are shown in Figure 5a. Because a polyacrylic acid ester polymer is a non-crystalline solid with no fixed crystal structure, PA showed a broad peak before and after modification. The peak position of Ni-MOF-74@PA-PEI was consistent with the characteristic peak position of Ni-MOF-74, indicating both that PA did not affect the crystal structure of Ni-MOF-74 and the successful loading of Ni-MOF-74 on PA. The sharp peaks indicated good crystallinity of Ni-MOF-74 in the composite material. The characteristic peak width of Ni-MOF-74@PA-PEI was more notable than that of Ni-MOF-74 powder because the Ni-MOF-74 crystal in the composite material was smaller than that of the powder [36]. The Fourier-transform infrared spectra of the samples are shown in Figure 5b. The three characteristic peaks of PA at 2976 cm⁻¹, 1735 cm⁻¹, and 1472 cm⁻¹ were attributed to the asymmetric stretching vibration of C-H, stretching vibration of C=O, and bending vibration of C-H, respectively [37]. After modification, the peaks of PA at 1151 cm⁻¹, 910 cm⁻¹, and 848 cm⁻¹ in the range of the epoxy group stretching vibration were substantially weakened, indicating that the structure of the epoxy group was destroyed [38]. A new peak appeared near 1574 cm⁻¹, corresponding to the range of the N-H bending vibration peak (1610–1500 cm⁻¹) and indicating that the PA matrix was successfully grafted with amine modification. In the infrared spectrum of Ni-MOF-74 and Ni-MOF-74@PA-PEI, the peak at 3369 cm⁻¹ corresponded to the O-H stretching vibration caused by the water vapor in the pore channel [25,39], and the characteristic peak at 1561 cm⁻¹ could be attributed to the C-O stretching vibration of the carboxyl ester group in H₂DOBDC. The absorption peaks at 1414 cm⁻¹ and 889 cm⁻¹ represented the C-C bond in the aromatic ring and bending vibration of the benzene ring, respectively [39,40]. Compared with Ni-MOF-74, the characteristic peak at 889 cm⁻¹ in the spectrum of Ni-MOF-74@PA-PEI was weakened. The epoxy group stretching vibration was observed initially at 848 cm⁻¹ in the spectra of PA, and the vibration of PA-PEI shifted to 814 cm⁻¹, indicating the coordination between the MOF and matrix material as well as the successful MOF grafting onto the PA-PEI [38].

The Ni-MOF-74@PA-PEI composite material exhibited a uniform spherical shape (Figure 6a). The polymer matrix surface contained pores ranging from 0.1 μm to 4 μm in diameter (Figure 6b). The interior mainly comprised large pores with diameters ranging from 2 μm to 10 μm and had interconnected through-hole structures formed by the contact between the dispersed phase droplets (Figure 6c). These structural characteristics enabled the easy penetration of the metal salt and ligand solutions and provided a sufficient space for the subsequent in-situ MOF growth. Modifying the polymer matrix with PEI did not alter its pore structure (Figure S1). The element mappings obtained from the energy dispersive X-ray spectroscopy revealed that the nickel ions were uniformly dispersed within the polymer matrix after impregnation (Figure S2). The individual crystals of Ni-MOF-74 had an irregularly aggregated size of 5–10 μm (Figure 6h,i), attributed to the crystal growth being faster than the nucleation [41]. The surface morphology of the Ni-MOF-74@PA-PEI composite material revealed the presence of rod-shaped crystals several hundred nanometres in length, and the surface pores were reduced to less than 1 μm. The interior comprised elongated one-dimensional rod-shaped crystals with lengths of

approximately 200–300 nm, arranged tightly and uniformly (Figure 6e–g). This finding is consistent with the one-dimensional hexagonal channel characteristics of MOF-74 [42].

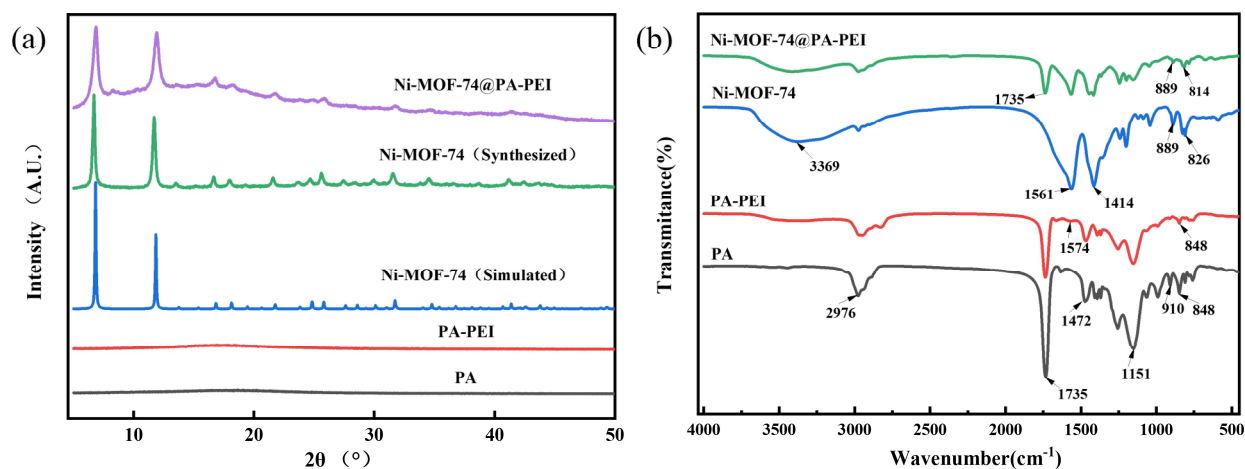


Figure 5. (a) X-ray diffraction patterns of PA, PA-PEI, Ni-MOF-74 (simulated and synthesized), and Ni-MOF-74@PA-PEI. (b) Fourier-transform infrared spectra of PA, PA-PEI, Ni-MOF-74, and Ni-MOF-74@PA-PEI.

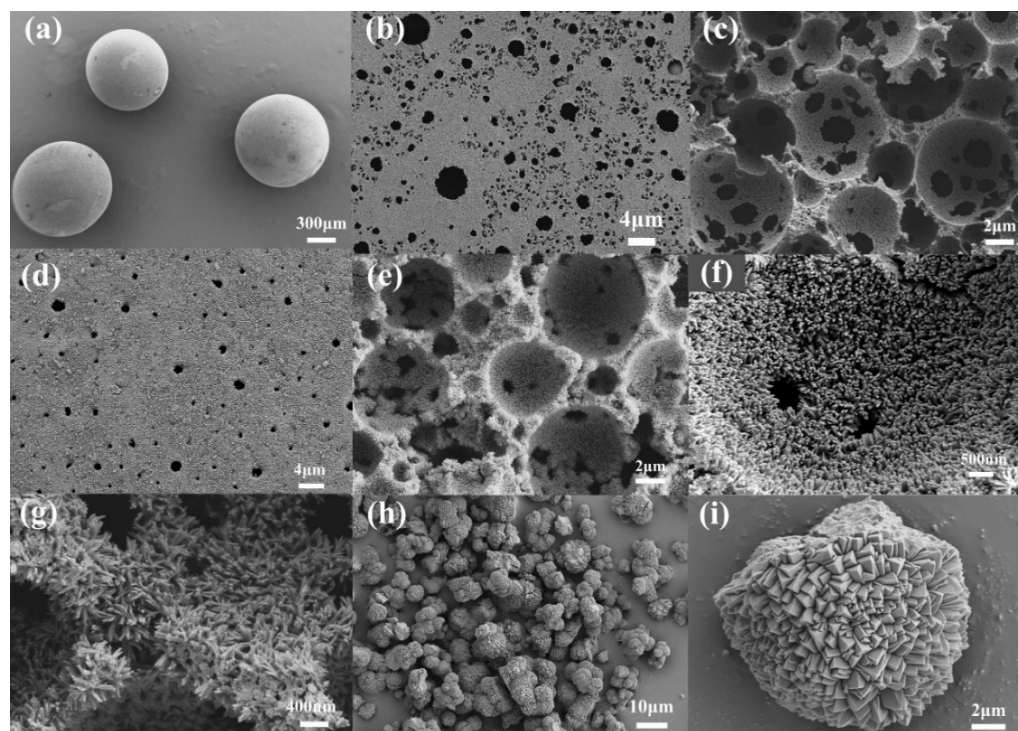


Figure 6. SEM images of (a) Ni-MOF-74@PA-PEI and (b) the PA surface. The internal pore structure of the (c) PA and (d) Ni-MOF-74@PA-PEI surface. The internal pore structure of (e–g) Ni-MOF-74@PA-PEI and (h,i) pristine Ni-MOF-74 at different magnifications.

The nano-sized Ni-MOF-74 was in-situ ordered grown within the PA matrix. Moreover, grafting amine modification enhanced the matrix surface energy and reduced the nucleation energy barrier, substantially decreasing the crystal nucleus size [43,44]. The transformation of the crystal shape from an irregular block shape to a long-rod shape was likely due to the introduction of the amino groups [31]. The composite still had pores on the surface and retained a through-hole structure inside, thereby facilitating the gas diffusion and mass transfer.

XPS was performed to confirm the composition of Ni–MOF–74 and PA, obtaining the results shown in Figure 7. Owing to the low concentration of Ni in the composite material and its magnetic nature, the XPS raw data of the composite material were weak and exhibited poor signal–to–noise ratios. However, the data fitting revealed that the Ni 2p spectrum of the materials could be deconvoluted into four characteristic peaks. Specifically, for Ni–MOF–74, the peaks at 856 eV and 860.83 eV were assigned to the Ni 2p_{3/2} main peak and its satellite peak, while those at 873.87 eV and 878.4 eV corresponded to the Ni 2p_{1/2} main peak and its satellite peak (Figure 7a) [45–47]. After composite formation with PA, the main peaks of Ni 2p_{3/2} and Ni 2p_{1/2} were located at 856.63 eV and 874.72 eV, respectively (Figure 7b). Compared with Ni–MOF–74, the two main peaks exhibited positive shifts of up to 0.63 eV and 0.85 eV, respectively, suggesting a decrease in the electron density around Ni and the occurrence of a coordination interaction between Ni and the modified matrix material. These results were consistent with the infrared spectroscopy data.

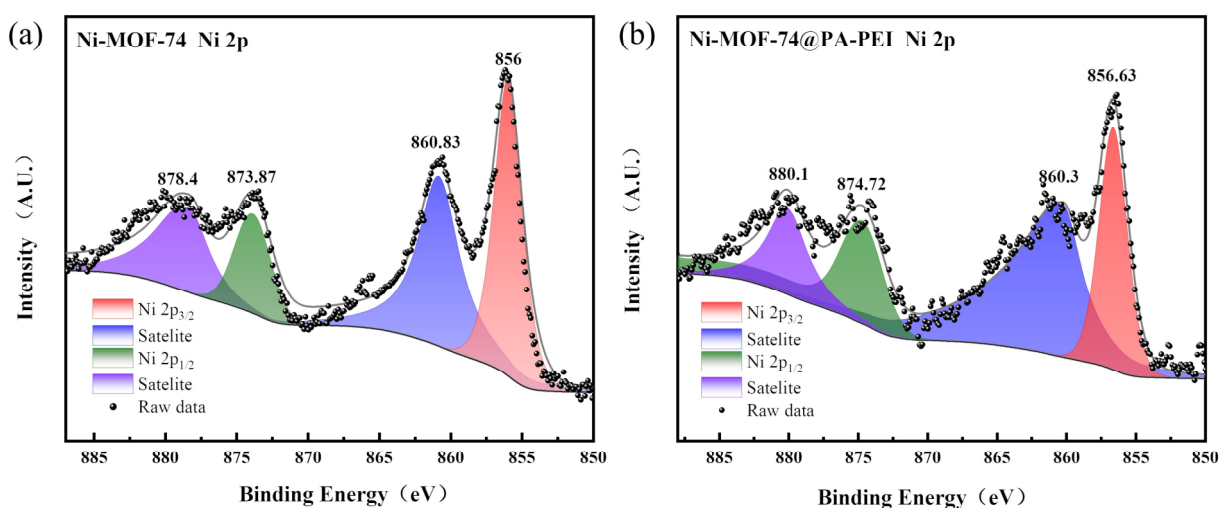


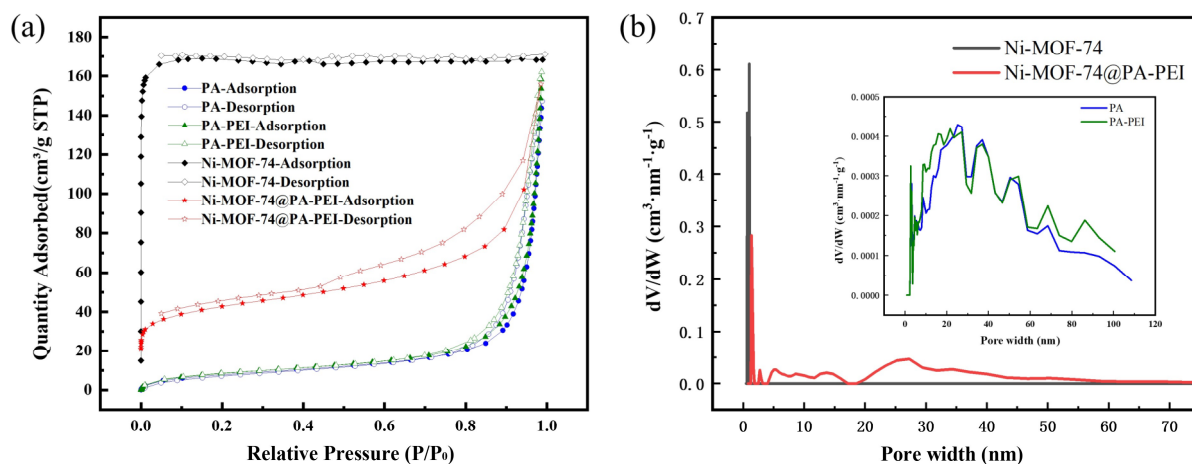
Figure 7. XPS spectra of Ni 2p for (a) Ni–MOF–74 and (b) Ni–MOF–74@PA–PEI.

3.2. Pore Structure Characteristics

The structural characteristic parameters and N₂ adsorption/desorption isotherms of PA, PA–PEI, Ni–MOF–74, and Ni–MOF–74@PA–PEI at 77 K are shown in Table 1 and Figure 8. The adsorption curve for the PA substrate material reflected a typical Type II isotherm, and its BET specific surface area was 30.3 m²/g. According to its pore size distribution (Figure 8b), the material mainly consisted of macropores and mesopores but no micropores. After modification, the adsorption curve and pore structure of PA did not change notably, being consistent with the SEM characterisation results. The adsorption isotherm of the synthesised Ni–MOF–74 reflected a typical Type I isotherm, with a BET specific surface area of 785.1 m²/g and total pore volume and average pore size of 0.26 cm³/g and 1.77 nm, respectively, agreeing with previous reports [25]. The adsorption isotherm of the Ni–MOF–74@PA–PEI composite material exhibited combined Type I and IV isotherms. In the low–pressure region, the adsorbate underwent capillary condensation, and the adsorption quickly increased, exhibiting a typical Type I adsorption isotherm. At $p/p_0 \approx 0.44$, desorption hysteresis occurred, exhibiting a typical Type IV isotherm of mesoporous solids. The BET–specific surface area of the composite material was 210.7 m²/g, while the microporous volume was 0.06 cm³/g, and the total pore volume was 0.24 cm³/g, indicating that the micropores accounted for 25% of the total pore volume. The loading of Ni–MOF–74 drastically reduced the size of the macropores in PA, while the composite material retained the microporous structure of Ni–MOF–74. This hierarchical pore structure was beneficial for the mass transfer and retention of the adsorbate.

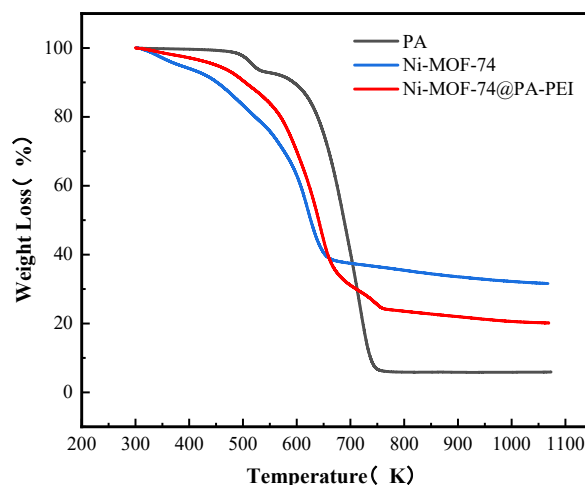
Table 1. Structural properties of the prepared materials.

Sample	Bulk Density (g/cm ³)	BET Surface Area (m ² /g)	Micropore Volume (cm ³ /g)	Pore Volume (cm ³ /g)	Average Pore Width (nm)
PA	0.18	30.3	–	0.09	12.82
PA–PEI	0.21	33.7	–	0.10	12.73
Ni–MOF–74	1.19	785.1	0.25	0.26	1.77
Ni–MOF–74@PA–PEI	0.32	210.7	0.06	0.24	6.29

**Figure 8.** (a) N₂ adsorption/desorption isotherms and (b) the pore size distribution of PA, PA–PEI, Ni–MOF–74, and Ni–MOF–74@PA–PEI.

3.3. Thermal Stability

The thermal stability test results of PA, Ni–MOF–74, and Ni–MOF–74@PA–PEI are shown in Figure 9. The highest stability was achieved by PA followed by Ni–MOF–74@PA–PEI and finally Ni–MOF–74. PA displayed two stages of weight loss, with a mass decrease of approximately 6% at 430–540 K, possibly owing to the decomposition of the unreacted monomers followed by a decrease in the mass above 650 K caused by the degradation of the polymer substrate [32]. For the Ni–MOF–74@PA–PEI composite material, the mass loss in the 300–423 K range could be attributed to the residual solvent molecules and pre-adsorbed gas. The Ni–MOF–74@PA–PEI composite exhibits a stability below 423 K, and is suitable for ambient temperature applications.

**Figure 9.** Thermal analysis results of PA, PA–PEI, Ni–MOF–74, and Ni–MOF–74@PA–PEI.

3.4. Radon Adsorption Capacity

The radon breakthrough curves for Ni–MOF–74 and Ni–MOF–74@PA–PEI are shown in Figure 10. The dynamic radon adsorption experiments were conducted under realistic ambient conditions of 293 K, relative humidity of 20%, and 1 bar. The pristine Ni–MOF–74 powder immediately penetrated and showed no Rn adsorption. This might be attributed to the damage of its pore structure because of tableting (Figure S3), resulting in a decrease in the adsorption capacity. For Ni–MOF–74@PA–PEI, to ensure sufficient gas–material interaction and avoid an excessive pressure drop, the tube was filled with approximately 80 mm of the composite material. The Rn concentration showed an immediate decrease after the material was introduced, reaching a minimum concentration of 1196 Bq/m³ after approximately 15 min and then gradually returning to its initial value. Based on fitting and calculations, the kinetic adsorption coefficient of the Ni–MOF–74@PA–PEI composite material was approximately 0.49 L/g. The radon adsorption coefficient of Ni–MOF–74@PA–PEI was from one to two orders of magnitude higher than that of zeolite and silica gel. Because Rn is an inert gas and its molecular dynamic diameter is 4.17 Å [48], radon is primarily combined with adsorbents through weak van der Waals forces with a lack of chemical reactivity. For Ni–MOF–74, its micropores were mainly distributed between 4.6 nm and 7.4 nm. Multiple research results have indicated a significant correlation between the Rn adsorption coefficient of a material and the number of 0.5–0.7 nm micropores [49–51]. We confirmed that Rn is preferentially adsorbed in pores within this range. Meanwhile, compared with the XRD of Ni–MOF–74@PA–PEI, the Ni–MOF–74@PA–PEI after radon breakthrough still maintained the corresponding characteristic peaks, but the peak intensity was slightly weakened (Figure S4). This could be attributed to the reduction of crystal phase content or the radioactivity of Rn during the testing process.

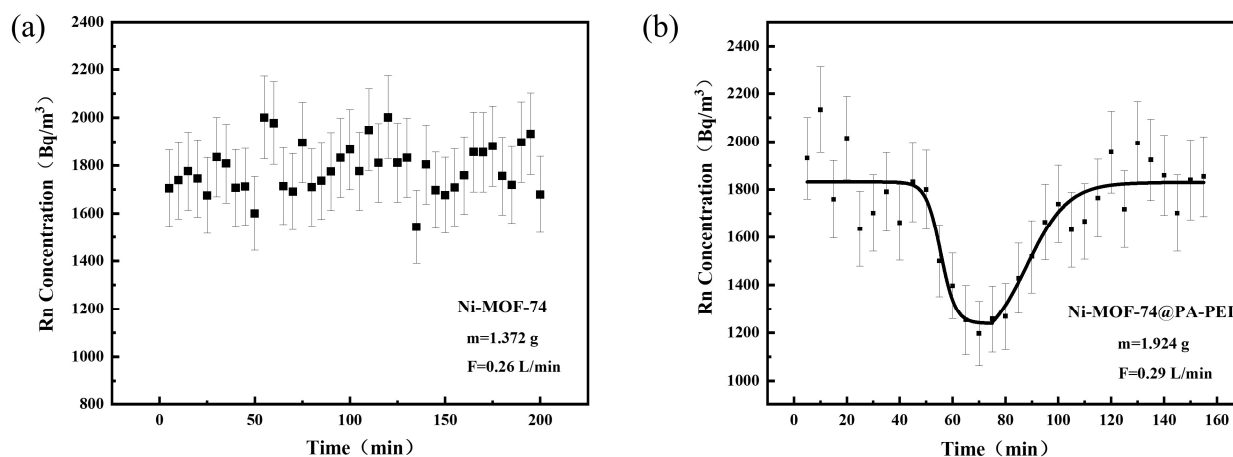


Figure 10. The radon breakthrough curve of (a) Ni–MOF–74 and (b) Ni–MOF–74@PA–PEI.

There is limited research on MOFs for radon adsorption, and this study was the first to investigate the effectiveness of Ni–MOF–74 for radon adsorption. Radon is a trace gas in the atmosphere with very low partial pressure ($<1.8 \times 10^{-14}$ bar, $<10^6$ Bq/m³) [22], and its adsorption coefficient by a material is highly dependent on humidity, temperature, and the carrier gas [9]. Furthermore, during radon removal, there is competition for adsorption between radon and other gases. Therefore, the deep removal of radon at ambient conditions remains challenging.

4. Conclusions

We prepared a modified spherical microporous polyester as the matrix material and achieved high–density, uniform in–situ growth of nanorod–shaped Ni–MOF–74 on its surface and inside through stepwise negative pressure impregnation. The amine–modified

matrix substantially reduced the surface nucleation energy barrier, and metal salt solution pre-impregnation provided a foundation for the subsequent ordered and dense growth of Ni-MOF-74. The characterisations showed that the Ni-MOF-74@PA-PEI composite material had a multilevel pore structure that was conducive to the mass transfer and adsorption. Based on these findings, we explored the Rn adsorption performance of both the pristine and composite material. Compared with the pristine Ni-MOF-74 powder, the prepared Ni-MOF-74@PA-PEI exhibited a better radon adsorption performance with an adsorption coefficient of 0.49 L/g (293 K, relative humidity of 20%, 1 bar). The microporous structure of Ni-MOF-74 demonstrated a certain ability to remove radon from the environment.

Our study confirmed the feasibility of in-situ growth of Ni-MOF-74 on polymer matrices such as polyacrylate and established a new composite material system that can be used for radon adsorption. Our development dramatically reduces the gas resistance during adsorption and opens new avenues for research on the practical use of MOFs for controlling radon concentrations.

Supplementary Materials: The following supporting information can be downloaded at: <https://www.mdpi.com/article/10.3390/pr11041069/s1>, Figure S1. Internal pore structure of PA-PEI, Figure S2. SEM/energy dispersive X-ray spectroscopy mappings of interior of Ni-MOF-74@PA-PEI, Figure S3. N₂ adsorption/desorption isotherms of Ni-MOF-74 (after tableting), Figure S4. X-ray diffraction patterns of several materials.

Author Contributions: Conceptualization, L.L. and Y.S.; methodology, X.L.; validation, X.L. and Y.L.; formal analysis, Y.L.; investigation, X.L. and L.L.; resources, Y.S. and C.W.; data curation, X.L. and C.W.; writing—original draft preparation, X.L.; writing—review and editing, X.L. and Y.S.; visualization, X.L.; supervision, L.L. and Y.L.; project administration, L.L.; funding acquisition, Y.S. and C.W. All authors have read and agreed to the published version of the manuscript.

Funding: This research was funded by the Fundamental Research Funds from the State Key Laboratory of NBC Protection for Civilian (SKLNBC 2021-06, SKLNBC 2021-07), China.

Data Availability Statement: Not applicable.

Acknowledgments: The authors gratefully acknowledge the financial support from the Fundamental Research Funds from State Key Laboratory of NBC Protection for Civilian (SKLNBC2021-06, SKLNBC2021-07), China.

Conflicts of Interest: The authors declare no conflict of interest.

References

1. Lei, B.; Zhao, L.; Girault, F.; Cai, Z.; Luo, C.; Thapa, S.; She, J.; Perrier, F. Overview and Large-Scale Representative Estimate of Radon-222 Flux Data in China. *Environ. Adv.* **2022**, *11*, 100312. [[CrossRef](#)]
2. Lorenzo-González, M.; Torres-Durán, M.; Barbosa-Lorenzo, R.; Provencio-Pulla, M.; Barros-Dios, J.M.; Ruano-Ravina, A. Radon Exposure: A Major Cause of Lung Cancer. *Expert Rev. Respir. Med.* **2019**, *13*, 839–850. [[CrossRef](#)] [[PubMed](#)]
3. Taylor, B.K.; Smith, O.V.; Miller, G.E. Chronic Home Radon Exposure Is Associated with Higher Inflammatory Biomarker Concentrations in Children and Adolescents. *Int. J. Environ. Res. Public Health* **2022**, *20*, 246. [[CrossRef](#)] [[PubMed](#)]
4. Ngoc, L.T.N.; Park, D.; Lee, Y.-C. Human Health Impacts of Residential Radon Exposure: Updated Systematic Review and Meta-Analysis of Case-Control Studies. *Int. J. Environ. Res. Public Health* **2022**, *20*, 97. [[CrossRef](#)]
5. Aprile, E.; Aalbers, J.; Agostini, F.; Alfonsi, M.; Amaro, F.D.; Anthony, M.; Antunes, B.; Arneodo, F.; Balata, M.; Barrow, P.; et al. The XENON1T Dark Matter Experiment. *Eur. Phys. J. C* **2017**, *77*, 881. [[CrossRef](#)]
6. O'Brien, P. *Optimization of Processing Parameters and Development of a Radon Trapping System for the NEWS-G Dark Matter Detector*; University of Alberta: Edmonton, AB, Canada, 2021.
7. Araujo, G.R.; Baudis, L.; Biondi, Y. The Upgraded Low-Background Germanium Counting Facility Gator for High-Sensitivity γ -Ray Spectrometry. *J. Inst.* **2022**, *17*, P08010. [[CrossRef](#)]
8. Finne, I.E.; Kolstad, T.; Larsson, M.; Olsen, B.; Prendergast, J.; Rudjord, A.L. Significant Reduction in Indoor Radon in Newly Built Houses. *J. Environ. Radioact.* **2019**, *196*, 259–263. [[CrossRef](#)]
9. Ackley, R.D. *Removal of Radon-220 from HTGR Fuel Reprocessing and Refabrication Off-Gas Streams by Adsorption (Based on a Literature Survey)*; Oak Ridge National Laboratory: Oak Ridge, TN, USA, 1975.
10. Bikit, I.; Mrdja, D.; Bikit, K.; Grujic, S.; Knezevic, D.; Forkapic, S.; Kozmidis-Luburic, U. Radon Adsorption by Zeolite. *Radiat. Meas.* **2015**, *72*, 70–74. [[CrossRef](#)]

11. Karunakara, N.; Sudeep Kumara, K.; Yashodhara, I.; Sahoo, B.K.; Gaware, J.J.; Sapra, B.K.; Mayya, Y.S. Evaluation of Radon Adsorption Characteristics of a Coconut Shell-Based Activated Charcoal System for Radon and Thoron Removal Applications. *J. Environ. Radioact.* **2015**, *142*, 87–95. [[CrossRef](#)]
12. Pushkin, K.; Akerlof, C.; Anbajagane, D.; Armstrong, J.; Arthurs, M.; Bringewatt, J.; Edberg, T.; Hall, C.; Lei, M.; Raymond, R.; et al. Study of Radon Reduction in Gases for Rare Event Search Experiments. *Nucl. Instrum. Methods Phys. Res. Sect. A Accel. Spectrometers Detect. Assoc. Equip.* **2018**, *903*, 267–276. [[CrossRef](#)]
13. Deng, X.; Yu, B.; Wu, H.; He, Z.; Wang, M.; Xiao, D. High-Efficiency Radon Adsorption by Nickel Nanoparticles Supported on Activated Carbon. *New J. Chem.* **2022**, *46*, 9222–9228. [[CrossRef](#)]
14. Fajt, L.; Kouba, P.; Mamedov, F.; Smolek, K.; Štekl, I.; Fojtík, P.; Hýža, M.; Hülka, J.; Jílek, K.; Stoček, P.; et al. Compact Anti-Radon Facility. In Proceedings of the Low Radioactivity Techniques 2015 (LRT 2015): Proceedings of the 5th International Workshop in Low Radioactivity Techniques, Seattle, WA, USA, 18–20 March 2015.
15. Furukawa, H.; Cordova, K.E.; O’Keeffe, M.; Yaghi, O.M. The Chemistry and Applications of Metal-Organic Frameworks. *Science* **2013**, *341*, 1230444. [[CrossRef](#)]
16. Perry, J.J.; Teich-McGoldrick, S.L.; Meek, S.T.; Greathouse, J.A.; Haranczyk, M.; Allendorf, M.D. Noble Gas Adsorption in Metal–Organic Frameworks Containing Open Metal Sites. *J. Phys. Chem. C* **2014**, *118*, 11685–11698. [[CrossRef](#)]
17. Banerjee, D.; Simon, C.M.; Elsaidi, S.K.; Haranczyk, M.; Thallapally, P.K. Xenon Gas Separation and Storage Using Metal-Organic Frameworks. *Chem* **2018**, *4*, 466–494. [[CrossRef](#)]
18. Pei, J.; Gu, X.-W.; Liang, C.-C.; Chen, B.; Li, B.; Qian, G. Robust and Radiation-Resistant Hofmann-Type Metal–Organic Frameworks for Record Xenon/Krypton Separation. *J. Am. Chem. Soc.* **2022**, *144*, 3200–3209. [[CrossRef](#)]
19. Van Heest, T.; Teich-McGoldrick, S.L.; Greathouse, J.A.; Allendorf, M.D.; Sholl, D.S. Identification of Metal–Organic Framework Materials for Adsorption Separation of Rare Gases: Applicability of Ideal Adsorbed Solution Theory (IAST) and Effects of Inaccessible Framework Regions. *J. Phys. Chem. C* **2012**, *116*, 13183–13195. [[CrossRef](#)]
20. Sumer, Z.; Keskin, S. Molecular Simulations of MOF Adsorbents and Membranes for Noble Gas Separations. *Chem. Eng. Sci.* **2017**, *164*, 108–121. [[CrossRef](#)]
21. Zeng, X.; Chen, F.; Cao, D. Screening Metal-Organic Frameworks for Capturing Radioactive Gas Rn in Indoor Air. *J. Hazard. Mater.* **2019**, *366*, 624–629. [[CrossRef](#)]
22. Wang, X.; Ma, F.; Liu, S.; Chen, L.; Xiong, S.; Dai, X.; Tai, B.; He, L.; Yuan, M.; Mi, P.; et al. Thermodynamics-Kinetics-Balanced Metal–Organic Framework for In-Depth Radon Removal under Ambient Conditions. *J. Am. Chem. Soc.* **2022**, *144*, 13634–13642. [[CrossRef](#)]
23. Wang, X.W.; Yan, T.; Wan, J.; Zhao, L.F.; Tu, Y. Zeolitic Imidazolate Framework-8 as a Nano-adsorbent for Radon Capture. *Nucl. Sci. Tech.* **2016**, *27*, 9. [[CrossRef](#)]
24. Chen, D.-L.; Shang, H.; Zhu, W.; Krishna, R. Transient Breakthroughs of CO₂/CH₄ and C₃H₆/C₃H₈ Mixtures in Fixed Beds Packed with Ni-MOF-74. *Chem. Eng. Sci.* **2014**, *117*, 407–415. [[CrossRef](#)]
25. Harandizadeh, A.H.; Aghamiri, S.; Hojjat, M.; Ranjbar-Mohammadi, M.; Talaie, M.R. Adsorption of Carbon Dioxide with Ni-MOF-74 and MWCNT Incorporated Poly Acrylonitrile Nanofibers. *Nanomaterials* **2022**, *12*, 412. [[CrossRef](#)] [[PubMed](#)]
26. Lei, L.; Cheng, Y.; Chen, C.; Kosari, M.; Jiang, Z.; He, C. Taming Structure and Modulating Carbon Dioxide (CO₂) Adsorption Isothermic Heat of Nickel-Based Metal Organic Framework (MOF-74(Ni)) for Remarkable CO₂ Capture. *J. Colloid Interface Sci.* **2022**, *612*, 132–145. [[CrossRef](#)] [[PubMed](#)]
27. Thallapally, P.K.; Grate, J.W.; Motkuri, R.K. Facile Xenon Capture and Release at Room Temperature Using a Metal–Organic Framework: A Comparison with Activated Charcoal. *Chem. Commun.* **2012**, *48*, 347–349. [[CrossRef](#)] [[PubMed](#)]
28. Ghose, S.K.; Li, Y.; Yakovenko, A.; Dooryhee, E.; Ehm, L.; Ecker, L.E.; Dippel, A.-C.; Halder, G.J.; Strachan, D.M.; Thallapally, P.K. Understanding the Adsorption Mechanism of Xe and Kr in a Metal–Organic Framework from X-Ray Structural Analysis and First-Principles Calculations. *J. Phys. Chem. Lett.* **2015**, *6*, 1790–1794. [[CrossRef](#)]
29. Riley, B.J.; Chong, S.; Kuang, W.; Varga, T.; Helal, A.S.; Galanek, M.; Li, J.; Nelson, Z.J.; Thallapally, P.K. Metal–Organic Framework–Polyacrylonitrile Composite Beads for Xenon Capture. *ACS Appl. Mater. Interfaces* **2020**, *12*, 45342–45350. [[CrossRef](#)]
30. Peterson, G.W.; Lee, D.T.; Barton, H.F.; Epps, T.H.; Parsons, G.N. Fibre-Based Composites from the Integration of Metal–Organic Frameworks and Polymers. *Nat. Rev. Mater.* **2021**, *6*, 605–621. [[CrossRef](#)]
31. Feng, W.; Wu, H.; Jin, J.; Liu, D.; Meng, H.; Yun, J.; Mi, J. Transformation of Al-CDC from 3D Crystals to 2D Nanosheets in Macroporous Polyacrylates with Enhanced CH₄/N₂ Separation Efficiency and Stability. *Chem. Eng. J.* **2022**, *429*, 132285. [[CrossRef](#)]
32. Nie, L.; Bai, L.; Chen, J.; Jin, J.; Mi, J. Grafting Poly(Ethyleneimine) on the Pore Surface of Poly(Glycidyl Methacrylate-Trimethylolpropane Triacrylate) for Preparation of the CO₂ Sorbent. *Energy Fuels* **2019**, *33*, 12610–12620. [[CrossRef](#)]
33. Yang, C.; Du, Z.; Jin, J.; Chen, J.; Mi, J. Epoxide-Functionalized Tetraethylenepentamine Encapsulated into Porous Copolymer Spheres for CO₂ Capture with Superior Stability. *Appl. Energy* **2020**, *260*, 114265. [[CrossRef](#)]
34. Chaudhary, V.; Sharma, S. Suspension polymerization technique: Parameters affecting polymer properties and application in oxidation reactions. *J. Polym. Res.* **2019**, *26*, 102. [[CrossRef](#)]
35. Wang, F.; Wang, H.; Ma, H.; Zhang, L.; Sun, C.; Guo, Q. Radon Dynamic Adsorption Coefficients of Two Activated Charcoals at Different Temperatures in Nitrogen Environment. *Appl. Radiat. Isot.* **2023**, *191*, 110564. [[CrossRef](#)]
36. Ungár, T. Microstructural Parameters from X-Ray Diffraction Peak Broadening. *Scr. Mater.* **2004**, *51*, 777–781. [[CrossRef](#)]

37. Guo, C.; Luo, X.; Zhou, X.; Shi, B.; Wang, J.; Zhao, J.; Zhang, X. Quantitative Analysis of Binary Polymorphs Mixtures of Fusidic Acid by Diffuse Reflectance FTIR Spectroscopy, Diffuse Reflectance FT-NIR Spectroscopy, Raman Spectroscopy and Multivariate Calibration. *J. Pharm. Biomed. Anal.* **2017**, *140*, 130–136. [[CrossRef](#)] [[PubMed](#)]
38. Guo, M.; Wu, H.; Lv, L.; Meng, H.; Yun, J.; Jin, J.; Mi, J. A Highly Efficient and Stable Composite of Polyacrylate and Metal–Organic Framework Prepared by Interface Engineering for Direct Air Capture. *ACS Appl. Mater. Interfaces* **2021**, *13*, 21775–21785. [[CrossRef](#)]
39. Sun, W.; Guo, J.; Ou, H.; Zhang, L.; Wang, D.; Ma, Z.; Zhu, B.; Ali, I.; Naz, I. Facile Synthesis of Highly Moisture-Resistant Mg-MOF-74 by Coating Hexagonal Boron Nitride (h-BN). *J. Solid State Chem.* **2022**, *311*, 123073. [[CrossRef](#)]
40. Liu, S.-F.; Hou, Z.-W.; Lin, L.; Li, F.; Zhao, Y.; Li, X.-Z.; Zhang, H.; Fang, H.-H.; Li, Z.; Sun, H.-B. 3D Nanoprinting of Semiconductor Quantum Dots by Photoexcitation-Induced Chemical Bonding. *Science* **2022**, *377*, 1112–1116. [[CrossRef](#)]
41. Wu, X.; Bao, Z.; Yuan, B.; Wang, J.; Sun, Y.; Luo, H.; Deng, S. Microwave Synthesis and Characterization of MOF-74 (M=Ni, Mg) for Gas Separation. *Microporous Mesoporous Mater.* **2013**, *180*, 114–122. [[CrossRef](#)]
42. Chen, T.; Wang, F.; Cao, S.; Bai, Y.; Zheng, S.; Li, W.; Zhang, S.; Hu, S.; Pang, H. In Situ Synthesis of MOF-74 Family for High Areal Energy Density of Aqueous Nickel–Zinc Batteries. *Adv. Mater.* **2022**, *34*, 2201779. [[CrossRef](#)]
43. Jiao, C.; Majeed, Z.; Wang, G.-H.; Jiang, H. A Nanosized Metal–Organic Framework Confined inside a Functionalized Mesoporous Polymer: An Efficient CO₂ Adsorbent with Metal Defects. *J. Mater. Chem. A* **2018**, *6*, 17220–17226. [[CrossRef](#)]
44. Crivello, C.; Sevim, S.; Graniel, O.; Franco, C.; Pané, S.; Puigmartí-Luis, J.; Muñoz-Rojas, D. Advanced Technologies for the Fabrication of MOF Thin Films. *Mater. Horiz.* **2021**, *8*, 168–178. [[CrossRef](#)]
45. Pan, Y.; Han, Y.; Chen, Y.; Li, D.; Tian, Z.; Guo, L.; Wang, Y. Benzoic Acid-Modified 2D Ni-MOF for High-Performance Supercapacitors. *Electrochim. Acta* **2022**, *403*, 139679. [[CrossRef](#)]
46. Wang, X.; Guan, D.; Li, F.; Li, M.; Zheng, L.; Xu, J. Magnetic and Optical Field Multi-Assisted Li–O₂ Batteries with Ultrahigh Energy Efficiency and Cycle Stability. *Adv. Mater.* **2022**, *34*, 2104792. [[CrossRef](#)]
47. Jayaramulu, K.; Masa, J.; Tomanec, O.; Peeters, D.; Ranc, V.; Schneemann, A.; Zboril, R.; Schuhmann, W.; Fischer, R.A. Nanoporous Nitrogen-Doped Graphene Oxide/Nickel Sulfide Composite Sheets Derived from a Metal–Organic Framework as an Efficient Electrocatalyst for Hydrogen and Oxygen Evolution. *Adv. Funct. Mater.* **2017**, *27*, 1700451. [[CrossRef](#)]
48. Chen, L.; Reiss, P.S.; Chong, S.Y.; Holden, D.; Jelfs, K.E.; Hasell, T.; Little, M.A.; Kewley, A.; Briggs, M.E.; Stephenson, A.; et al. Separation of rare gases and chiral molecules by selective binding in porous organic cages. *Nature Mater.* **2014**, *13*, 954–960. [[CrossRef](#)]
49. Wang, Q.; Qu, J.; Zhu, W.; Zhou, B.; Cheng, J. An Experimental Study on Radon Adsorption Ability and Microstructure of Activated Carbon. *Nucl. Sci. Eng.* **2011**, *168*, 287–292. [[CrossRef](#)]
50. Noël, R.; Busto, J.; Fierro, V. Measurements and Understanding of Radon Adsorption in Nanoporous Materials. In Proceedings of the Low Radioactivity Techniques 2015 (LRT 2015): Proceedings of the 5th International Workshop in Low Radioactivity Techniques, Seattle, WA, USA, 18–20 March 2015.
51. Liu, L.; Deng, X.; Liao, Y.; Xiao, D.; Wang, M. Activated Carbon/Attapulgite Composites for Radon Adsorption. *Mater. Lett.* **2021**, *285*, 129177. [[CrossRef](#)]

Disclaimer/Publisher’s Note: The statements, opinions and data contained in all publications are solely those of the individual author(s) and contributor(s) and not of MDPI and/or the editor(s). MDPI and/or the editor(s) disclaim responsibility for any injury to people or property resulting from any ideas, methods, instructions or products referred to in the content.